ELSEVIER

Contents lists available at ScienceDirect

Journal of Catalysis

journal homepage: www.elsevier.com/locate/jcat



Effects of diffusional constraints on lifetime and selectivity in methanol-to-olefins catalysis on HSAPO-34



Andrew Hwang a,1, Thuy T. Le b,1, Zhichen Shi a, Heng Dai b, Jeffrey D. Rimer b,*, Aditya Bhan a,*

ARTICLE INFO

Article history: Received 15 August 2018 Revised 3 October 2018 Accepted 25 October 2018

Keywords:
Complex reaction network
MTO
Diffusional constraints
Crystallite size
Site density
Si speciation
Zeotype

ABSTRACT

Reaction-transport formalisms show that the effects of crystallite size, H⁺ density, and Si speciation of HSAPO-34 on catalyst lifetime and selectivity in methanol-to-olefins catalysis are all manifestations of diffusional constraints. Both structural catalyst properties-i.e., crystallite size and H+ density-and intrinsic kinetic constants (per H⁺)-regulated, in silicoaluminophosphates, by Si speciation-affect the severity of these diffusional restrictions. Methanol-to-olefins catalysis on HSAPO-34 occurs by a complex network of autocatalytic reactions in which temporal gradients persist along with spatial gradients inherent to continuous-flow, fixed-bed reactors. Invocation of reaction rates in the interpretation of lifetime and selectivity trends in such systems requires defined quantities averaged in both time and space because measured observables conflate instantaneous reaction rates with spatial and temporal gradients. Quantities defined herein, i.e., total turnovers and cumulative selectivity, provide such rigorous assessments of lifetime and selectivity that permit causative correlation between rates of reactions within the complex network of autocatalytic reactions and material properties of HSAPO-34. Total turnovers decreases with increasing diffusional constraints because dehydrocyclization reactions experience stronger diffusional constraints than olefins methylation, aromatics dealkylation, and methanol transfer hydrogenation. Cumulative selectivity to paraffins increases with increasing diffusional constraints because transfer hydrogenation reactions of methanol, ethylene, and propylene experience stronger diffusional constraints than all other reactions within the complex reaction network, The approaches detailed herein codify the chemical and physical origins of trends in process outcomes with system variables for reaction systems characterized by complex reaction networks and prevailing spatial and temporal concentration gradients.

© 2018 Elsevier Inc. All rights reserved.

1. Introduction

Complex reaction networks are ubiquitous; they arise in, e.g., biochemical systems [1], interstellar chemistry [2], combustion and pyrolysis [3], and heterogeneous catalysis [4]. The large number of species and reactions often preclude precise kinetic and mechanistic analysis of elementary steps that comprise the complex reaction network and, more often, restrict optimization of material properties and process parameters to maximize, e.g., catalyst lifetime and selectivity to heuristic approaches. Trends of catalyst lifetime and selectivity with material properties and process parameters must emerge, however, as consequences of the governing physical and chemical phenomena without regard for heuristics and with provenance linked inexorably to the complex reaction network.

Methanol-to-hydrocarbons catalysis on zeotypes and zeolites occurs via a complex reaction network; the species include oxygenates and acyclic and cyclic and aliphatic and aromatic hydrocarbons, and the reactions include methylation, oligomerization, hydrogen transfer, cyclization, β -scission, and dealkylation [5–8]. The use of small-pore zeotypes/zeolites-e.g., in methanol-toolefins catalysis on HSAPO-34, a small-pore silicoaluminophosphate (SAPO) zeotype with CHA topology [9,10]-adds further complexity because species engaged in the reaction networknamely, branched aliphatics and aromatics-remain entrained within the zeotype/zeolite cavities during catalysis [11,12] and rapid catalyst deactivation [5-7,13-15] imposes persistent temporal gradients on continuous-flow reactors. The chemical origins of the effects of methanol space velocity and methanol concentration, i.e., process parameters, on catalyst lifetime and selectivity in methanol-to-olefins catalysis trace to methanol dehydrogenation [16–19]. The physical and chemical origins of the effects of crystallite size, H⁺ density, and Si speciation, i.e., material properties of

^a Department of Chemical Engineering and Materials Science, University of Minnesota, Minneapolis, MN 55455, USA

^b Department of Chemical and Biomolecular Engineering, University of Houston, Houston, TX 77204, USA

^{*} Corresponding authors.

E-mail addresses: jrimer@central.uh.edu (J.D. Rimer), abhan@umn.edu (A. Bhan).

¹ These authors contributed equally to this work.

HSAPO-34, on catalyst lifetime and selectivity remain, despite numerous investigations [14,20–32], unresolved. For example, previous reports attribute, with apparent conflict, trends of catalyst lifetime with crystallite size to product shape selectivity [24], transition state selectivity [22,28], external surface acid site density [29], and mass transport properties [27,29,31].

Here, we report the preparation of HSAPO-34 formulations diverse in morphology and composition; the characterization of crystallite size, H⁺ density, and Si speciation; and trends of lifetime and selectivity in methanol-to-olefins catalysis with these material properties. Reaction-transport formalisms show that effects of crystallite size, H⁺ density, and Si speciation on lifetime and selectivity manifest together as consequences of diffusional constraints. Interpretation of trends in lifetime and selectivity within the context of this reaction-transport formalism reveals that specific classes of reactions, within the complex reaction network, experience stronger diffusional constraints than others. Lifetime. assessed here as total turnovers, decreases with increasing diffusional constraints because dehydrocyclization reactions producing entrained hydrocarbons experience stronger diffusional constraints than reactions producing light olefins. Methane, ethane, and propane selectivities increase with increasing diffusional constraints because transfer hydrogenation reactions of methanol, ethylene, and propylene experience stronger diffusional constraints than reactions producing light olefins. These results provide guidance, founded on principles of transport phenomena and reaction engineering, on material properties necessary to maximize lifetime and light olefins selectivity in methanol-to-olefins catalysis. More broadly, the methodology, results, and discussion herein represent a case-study on the assessment of physical and chemical origins of lifetime and selectivity trends for complex reaction networks in heterogeneous catalytic processes with both temporal and spatial concentration gradients.

2. Experimental methods

2.1. Materials synthesis

Colloidal silica (c-SiO₂; LUDOX[®] HS-40), fumed silica (f-SiO₂; Cab-O-Sil[®] M-5), aluminum isopropoxide (Al(OⁱPr)₃; 98 wt%,

Aldrich), boehmite (AlO(OH); 72%, Catapal B[®], Sasol), phosphoric acid (H₃PO₄; 85%, Sigma–Aldrich), tetraethylammonium hydroxide (TEAOH; 35%, Sigma–Aldrich), morpholine (MP; \geq 99%, Sigma–Aldrich), and triethylamine (Et₃N; \geq 99%, Sigma–Aldrich) were used as received without further purification. Deionized water was purified with an Aqua Solutions Type I RODI filtration system (18.2 M Ω).

SAPO-34 samples were prepared by adapting reported protocols; the synthesis conditions for all samples are summarized in Table 1. Solution compositions starting with Si/(Si + Al + P) \leqslant 0.108 and SiO₂/Al₂O₃ within 0.075–0.15 were selected based on reported criteria [33,34] to achieve SAPO-34 crystals with uniquely isolated Si speciation, i.e., Si(OAl)₄, and avoid formation of siliceous domains [35]. Crystallization times were also adjusted to control Si speciation [36]. Organic structure-directing agents were selected to control crystallite size as, in general, TEAOH-directed crystallization gives submicron crystallites while MP- and Et₃N-directed crystallization give \geqslant 1 µm crystallites [37,38]. See Section S1 of the Supporting Information for more discussion on the effects of synthesis conditions on Si speciation and crystallite size and morphology.

In a typical synthesis [42], a 22 g mixture with a molar composition of

 $1Al_2O_3 : xSiO_2 : 3P_2O_5 : 6TEAOH : 108H_2O$

(with x = 0.15-0.6) was prepared. Al(OⁱPr)₃ was added to deionized water followed by c-SiO₂ and then TEAOH. The mixture was stirred in a 65 mL polypropylene bottle for 2 h at ambient temperature to dissolve the Al and Si sources. H₃PO₄ was then added dropwise over an interval of 0.5–1 h to avoid gelation. The resulting mixture was then aged for an additional period of time (0.5–24 h), transferred into a Teflon-lined stainless steel autoclave (Parr Instruments), and heated in a Thermo Fisher Precision oven at a specified crystallization temperature (438–473 K) with or without rotation under autogenous pressure for 6–48 h. The autoclaves were then removed from the oven and quenched in water to ambient temperature. The products were washed with deionized water via three cycles of centrifugation (Beckman Coulter Avanti J-E)–10 min cycles at 278 K and 13,000 rpm. The supernatant was decanted, and the washed samples were dried overnight at 323 K. SAPO-34 samples were

Table 1 Synthesis conditions for preparation of SAPO-34 samples.

Sample	OSDA ^d	Solution composition	Precursor			Aging time/h	Temp./K	Time ^g /h
		Al ₂ O ₃ :SiO ₂ :P ₂ O ₅ :H ₂ O:osda	Al	Si	P			
1	TEAOHe	1:0.6:3:108:6	Al(O ⁱ Pr) ₃	c-SiO ₂	H ₃ PO ₄	2	453	6 ^h
2	TEAOH	1:0.6:3:108:6	$Al(O^iPr)_3$	c-SiO ₂	H_3PO_4	24	453	5
3	TEAOH	1:0.15:3:108:6	$Al(O^iPr)_3$	c-SiO ₂	H_3PO_4	0.5	453	48
4	TEAOH	1:0.6:3:108:6	$Al(O^iPr)_3$	c-SiO ₂	H_3PO_4	3	453	6 ^h
5	TEAOH	1:0.6:3:108:6	$Al(O^iPr)_3$	c-SiO ₂	H_3PO_4	1.5	473	4
6 ^a	TEAOH	1:0.1:1:63:2	$Al(O^iPr)_3$	c-SiO ₂	H_3PO_4	24	473	24 ^h
7 ^b	TEAOH + MPf	1:0.3:1:52: (0.7:1.3)	$Al(O^iPr)_3$	f-SiO ₂	H_3PO_4	24	453	24 ^h
8	TEAOH + MP	1:0.3:1:52: (0.7:1.3)	$Al(O^iPr)_3$	f-SiO ₂	H_3PO_4	24	453	24 ^h
9€	Et ₃ N ⁱ	1:0.44:1.1:35:2.3	AlO(OH)	c-SiO ₂	H_3PO_4	24	438	33 ^h
10	TEAOH	1:0.6:3:108:6	$Al(O^{i}Pr)_{3}$	c-SiO ₂	H_3PO_4	0.5	473	24
11	TEAOH	1:0.6:3:108:6	$Al(O^iPr)_3$	c-SiO ₂	H ₃ PO ₄	24	453	24 ^h
12	TEAOH	1:0.6:3:108:6	$Al(O^iPr)_3$	c-SiO ₂	H ₃ PO ₄	0.5	453	20 ^h
13	TEAOH	1:0.6:3:108:6	$Al(O^iPr)_3$	c-SiO ₂	H ₃ PO ₄	24	453	6

^a Protocol adapted from Ref. [39].

^b Seeded syntheses with 3 wt% seed (sample 9) based on amount of Si in starting solution.

^c Protocol adapted from Ref. [40,41].

^d Organic structure-directing agent.

^e Tetraethylammonium hydroxide.

f Morpholine.

g Crystallization time.

h Synthesized in rotation oven.

ⁱ Triethylamine.

stored with the cationic moiety of the organic structure-directing agent intact to avoid modifications to Si speciation upon exposure to ambient moisture [43]. SAPO-34 samples were converted to H^{\dagger} -form via thermal oxidative treatment on stream immediately prior to catalytic testing (*vide infra*).

2.2. Structural and chemical characterization

Powder X-ray diffraction was used to characterize the crystal structure and phase purity of as-synthesized SAPO-34 samples. X-ray diffraction patterns were collected on a Rigaku SmartLab Diffractometer using Cu K α radiation (40 kV, 30 mA) in the range of 2θ = 5–50 degrees with 0.02 degree increments. The collected patterns were compared against a reference CHA pattern obtained from the International Zeolite Association [44].

Scanning electron micrographs were collected using a LEO Gemini 1525 Field Emission Scanning Electron Microscope equipped with a Schottky field emission gun. SAPO-34 samples were prepared for imaging by depositing powders on carbon tape and coating them with a thin layer of carbon to prevent charging effects during image collection.

Dynamic light scattering was used to assess the crystallite size of submicron SAPO-34 samples. A sample was diluted in deionized water and placed in a clean glass vial; the level of dilution was adjusted to ensure a scattering count rate within 30,000–100,000 kilocounts per second. The glass vial was placed in a decalin bath (298 K) sample holder housed within a Brookhaven Instruments BI-200SM system equipped with a HeNe laser (637 nm) and Turbo-Corr Digital Correlator. A total of six measurements at 298 K were taken for each sample (2 min per measurement), and the measured autocorrelation functions were analyzed using the method of cumulants to obtain an average hydrodynamic diameter and polydispersity index.

Transient sorption of propane (Matheson, 99.999%) on HSAPO-34 was performed using a gas adsorption system (Micromeritics ASAP 2020) equipped with a high vacuum pump and a 1 mmHg pressure transducer (1 µmHg resolution). As-synthesized SAPO-34 powders were crushed, pelletized, and sieved to obtain (180-250 μm) aggregates and then detemplated and converted to H⁺form via thermal oxidative treatment (vide infra). HSAPO-34 aggregates (0.050-0.10 g) were loaded into a quartz tube which was then attached to the gas adsorption system; the sample was evacuated ($\leq 6 \,\mu\text{mHg}$) at 673 K for 4 h (0.0167 K s⁻¹) and then cooled to adsorption temperature (333 K) under vacuum prior to acquisition of transient sorption data. The evacuated sample was isolated from the gas manifold which was then pressurized with known amounts of propane ($P = 10^2 - 10^3$ mmHg, T = 319 K). The sample was then exposed to the gas manifold, and the pressure was recorded as a function of time $(t_n - t_{n-1} = 2-20 \text{ s})$ until equilibrium $(\delta P = P(t_{n_{eq}}) - P(t_{n_{eq}-1}) < 0.1 \text{ mmHg})$ was established. The cycle of sample isolation, manifold dosing, and transient sorption was repeated until transient sorption data with sufficiently low overall pressure changes ($\Delta P = P(t_{n_{eq}}) - P(t = 0) \lesssim 20\%$) were collected.

 N_2 adsorption isotherms were measured (Micromeritics ASAP 2020) at 77 K and used to calculate micropore volumes using the t-plot method [45]. HSAPO-34 samples were treated in vacuum ($\leq 6 \ \mu mHg$) at 673 K for 4 h (0.0167 K s $^{-1}$) prior to acquisition of equilibrium N_2 adsorption data.

 NH_3 temperature programmed desorption was used to measure H^+ densities of SAPO-34 samples [46]. HSAPO-34 (0.050–0.10 g) was converted to NH_4^+ form by treatment in flowing 800 ppm NH_3 (1.01% NH_3 /He Praxair, certified standard), balanced by He (Minneapolis Oxygen, 99.997%) and Ar (Matheson, 99.9995%; internal standard), at 423 K until complete NH_3 breakthrough was observed using online mass spectrometry (MKS Cirrus 2,

 $m/z=16,\,17,\,40$). Weakly bound ammonia was removed by treating the NH $_4^+$ -exchanged SAPO-34 in flowing He (3.33 cm 3 s $^{-1}$ g $^{-1}$) at 423 K for $\geqslant 4$ h. The sample was heated rapidly in flowing He and Ar to 823 K (0.167 K s $^{-1}$) while the NH $_3$ evolved was measured using online mass spectrometry. H $^+$ densities were calculated by assuming unit stoichiometry between H $^+$ and NH $_3$ evolved.

 27 Al, 29 Si, 31 P MAS NMR spectra were recorded on a Bruker Avance 600 MHz spectrometer equipped with a 3.2 mm probe at resonance frequencies of 156.4, 119.3 and 243.0 MHz, respectively; using 3, 6.25, and 4 μs pulses, respectively; and 0.25, 120, and 10 s repetition times, respectively. The flip angle was $\pi/4$ for all nuclei; the spinning frequency was 15 kHz for 27 Al and 31 P and 10 kHz for 29 Si. The chemical shifts in 27 Al, 29 Si, 31 P spectra were referenced to Na₃AlF₆, Si(CH₃)₄, and H₃PO₄, respectively.

2.3. Catalytic testing

Methanol-to-olefins reactions were performed on fixed-beds comprised of HSAPO-34 aggregates (180–250 µm, 0.010–0.050 g) mixed with quartz granules (180-250 µm, 0.25-0.50 g; washed with 2 M HNO₃, rinsed with excess deionized water, and treated in flowing dry air at 1273 K for 12 h). Fixed-beds were supported between inert quartz wool plugs in a tubular quartz reactor (4 mm i.d.). The reactor was placed in a resistively heated furnace (National Element FA120), and the temperature was monitored by a K-type thermocouple (Omega) attached to the external walls of the reactor near the axial center of the fixed-bed and regulated by an electronic controller (Watlow 96). Fixed-beds were treated in flowing air (Matheson, Ultra Zero Certified) at 873 K (0.0167 K s⁻¹) for 6 h and cooled to reaction temperature (673 K) prior to catalytic testing. Liquid methanol (Fluka, 99.9%) was delivered by a syringe pump (Cole-Parmer 780100C) and vaporized into heated gas transfer lines (\geq 393 K). He and N₂ (Matheson, 99.999%; internal standard) flows were metered by thermal mass flow controllers (Brooks 5850). Concentrations of species comprising influent and effluent gas mixtures were quantified using gas chromatography (Agilent 7890) with parallel thermal conductivity (Porapak Q, 13 ft \times 1/8 in, 100–80 mesh) and flame ionization (HP-PLOT Q, 30 m \times 0.530 mm \times 40 μ m) detection.

3. Results and discussion

3.1. Preparation and characterization of SAPO-34 samples

Table 2 summarizes the characterization results for the catalog of SAPO-34 samples diverse in morphology, crystallite size, H^{+} density, and Si speciation. The samples were prepared by adapting reported protocols using various organic structure-directing agents; solution compositions; Si, Al, and P sources; aging times; and crystallization temperatures and times (Table 1 summarizes the synthesis conditions). Powder X-ray diffractograms confirm crystallization of the CHA topology (see Fig. S1 of the Supporting Information), and micropore volumes (Table 2) calculated from measured $N_{\rm 2}$ adsorption isotherms at 77 K are consistent with CHA-type materials.

3.1.1. Al, Si, and P speciation via MAS NMR

The Brønsted-acid function of microporous, crystalline SAPOs emanates from charge-balancing protons localized at O atoms bridging tetrahedrally coordinated Al and Si atoms [9]. Si incoporation into neutral aluminophosphates occurs via two mechanisms: (i) substitution of Si for P and (ii) substitution of a Si-Si pair for an Al-P pair [9,35,47]. Brønsted acid sites are localized at O atoms bridging Al and either an isolated Si (i.e., Si(OAl)₄), Si on the borders of siliceous islands, or Si in aluminosilicate regions within

Table 2Micropore volume, Si(OAl)₄ fraction, H* density, and size assessments of HSAPO-34 samples.

Sample ^a	$V_{\rm micro}^{} {\rm cm}^3 {\rm g}^{-1}$	Si(OAl) ₄ °/%	$\rho_{\mathrm{H}^+}^{\circ}{}^{\mathrm{d}}/(\mathrm{mol}_{\mathrm{H}^+}\mathrm{nm}^{-3})$	L _{SEM} e/nm	$L_{\rm DLS}^{\rm f}/{\rm nm}$	$D/R^{2g}/\mathrm{ks}^{-1}$	$\rho_{\rm H^+}^{\circ}({\it R}^2/{\it D})/({\rm mol_{H^+}ksnm^{-3}})$
1	0.28	100	0.59	_	260	2.9	0.21
2	0.27	100	0.56	480	_	2.0	0.28
3	0.28	100	0.71	150	_	2.2	0.32
4	0.28	100	0.74	_	490	2.0	0.36
5	0.25	100	0.83	510	_	1.8	0.47
6	0.26	100	0.79	1500	_	0.49	1.6
7	0.26	100	0.90	7700	_	0.30	3.0
8	0.27	100	0.86	12000	_	0.23	3.7
9	0.26	100	0.89	9200	_	0.12	7.3
10	0.30	76	0.98	1200	_	4.6	0.21
11	0.26	86	0.78	_	360	3.0	0.26
12	0.29	83	0.75	_	620	1.7	0.44
13	0.24	86	0.93	460	_	1.2	0.77

- ^a Sample numbers correspond to entries in Table 1.
- b t-plot method on measured N₂ adsorption isotherms at 77 K.
- ^c Integration of Bloch decay ²⁹Si MAS NMR spectra (Fig. 1).
- d NH₃ evolution upon thermal treatment of NH₄-exchanged samples.
- ^e Arithmetic mean of ≥30 crystallites from scanning electron micrographs (Fig. S3).
- f Cumulant analysis of autocorrelation functions measured in dynamic light scattering,
- g Transient sorption of propane at 333 K.

siliceous islands [35]. The first arises from Si incorporation mechanism (i), and the latter two arise from mechanism (ii) [35]. The proton affinity of the conjugate base is sensitive to the local coordinative environment of Si [33,48], and these variances in proton affinity, i.e., acid strength, manifest differences in catalysis [28,49] and reveal themselves in infrared spectra with appropriate probe molecules [50]. The Si speciation is affected by hydrothermal synthesis conditions, e.g., template identity [51] and gel composition [34], post-synthetic thermal [52] and hydrothermal [53] treatments, and exposure to ambient moisture [43,54]. Si speciation is typically identified using ²⁹Si MAS NMR [50,55-57] and quantified in Bloch decay spectra [28,51,58,59]. Fig. 1 shows the Bloch decay ²⁹Si MAS NMR spectra for as-synthesized SAPO-34 samples 1–13 in Table 2. The spectra for samples 1-9 (Table 2) show a single resonance at -92 ppm attributed to isolated, tetrahedrally coordinated Si in the SAPO-34 framework [51,56–58], i.e., Si(OAl)₄. The spectra for samples 10-13 (Table 2) show an additional resonance at −96 ppm attributed to Si(OAl)₃(OSi)₁ indicative of the formation of siliceous islands [28,50,51,58,59]. Table 2 lists the fractions of Si(OAl)₄ species in each sample as determined by integration of the Bloch decay ²⁹Si MAS NMR spectra.

The 27 Al MAS NMR spectra (Fig. S2a of the Supporting Information) show a resonance at 39 ppm attributed to tetrahedrally coordinated Al in the SAPO-34 framework [51,56–58] and a minor feature at 10–13 ppm (\leq 10% via integration of Bloch decay spectra) attributed to pentacoordinated Al arising from interactions between cationic moieties of the organic structure-directing agent, mineralizing agents, or water with tetrahedrally coordinated, framework Al [51,56,58]. The 31 P MAS NMR spectra (Fig. S2b of the Supporting Information) show a resonance at -29 ppm attributed to tetrahedrally coordinated P in the SAPO-34 framework [51,56–58], i.e., P(OAl)₄, and a minor feature at -13 ppm (\leq 5% via integration of Bloch decay spectra) attributed to P(OAl)₈(H₂O)₉ species [52,54]. These spectral results demonstrate that the SAPO-34 samples are devoid of extraframework Al and P species.

3.1.2. Assessment of H⁺ density

Table 2 lists the H⁺ densities of HSAPO-34 samples measured using NH₃ titration methods adapted from previously reported protocols [46]. The H⁺ count is normalized to the 36 T-atom CHA unit cell volume, 2391.6 Å³ per unit cell [10].

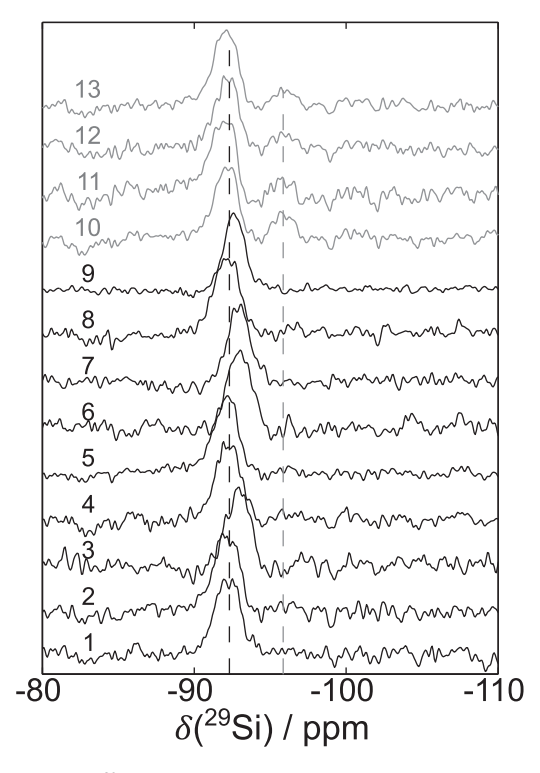


Fig. 1. Bloch decay 29 Si MAS NMR spectra of samples 1–9 and 10–13 in Table 2.

3.1.3. Assessments of size

The scanning electron micrographs (Fig. S3 of the Supporting Information) of samples 1–13 in Table 2 show that the crystallites exhibit plate and/or cubic morphology and size distributions ranging from nearly monodisperse (e.g., samples 7 and 8) to polydisperse (e.g., samples 3 and 5). Table 2 lists the crystallite sizes measured from scanning electron micrographs (arithmetic mean of \geqslant 30 crystallites, L_{SEM}) and determined from cumulant analysis of autocorrelation functions measured via dynamic light scattering [60] (L_{DLS}). One-dimensional assessments of size from electron microscopy and dynamic light scattering, however, conceal morphological discrepancies and disregard intracrystalline defects that affect dynamics of physical and chemical phenomena [61].

Furthermore, assessments of average size from electron micrographs require arithmetic or geometric averaging which do not reflect the ensemble averages sensed in bulk measurements of dynamical phenomena [62]. Transient sorption [63–65], however, gives values for a combined parameter, D/R^2 (vide infra), as a functional assessment of ensemble averaged size sensitive to both morphological discrepancies and intracrystalline defects.

Fig. 2 shows transient sorption profiles for propane adsorption at 333 K for samples 1, 6, and 9 in Table 2. The equilibrium propane adsorption isotherms, at 333 K and 10^2-10^3 mmHg, show linear correlation between equilibrium adsorption uptake and sorbate pressure (Fig. S4 of the Supporting Information) implying ideal sorbate behavior (fugacity coefficients sufficiently close to unity) with diffusivities independent of concentration [63,64,66]. Fig. 2 shows the data and fitting results only for a subset of the sample catalog to aid readability; see Fig. S5 of the Supporting Information for graphical representation of the complete data set.

The solid lines in Fig. 2 are curves estimated by regression of data to model equations describing radial diffusion in a sphere under isobaric and isothermal conditions [63,64]. The selected conditions—sorbate, temperature, and pressures—for collection of transient sorption data result in \lesssim 20% pressure change between the initial and final (equilibrium) states. Measured transient sorption profiles are initially regressed to the following model equation [63,64].

$$\frac{M_t}{M_{\infty}} = 1 - \frac{6}{\pi^2} \sum_{n=1}^{\infty} \frac{1}{n^2} \exp\left(-\frac{D}{R^2} n^2 \pi^2 t\right),\tag{1}$$

where M_t is the molar uptake at time t, M_{∞} is the equilibrium molar uptake, D is the effective diffusion constant of propane at 333 K, and R represents a characteristic length scale for diffusion. This nonlinear regression gives an estimate of the model's single parameter, D/R^2 . Eq. (1) describes transient sorption in crystallites with sufficiently narrow size distribution. A sorption model adapted for polydisperse crystallites applies a Gaussian distribution of sizes [63,64],

$$\begin{split} \frac{M_t}{M_{\infty}} &= 1 - \frac{6}{\pi^2} \sum_{n=1}^{\infty} \frac{1}{n^2} \int_0^{\infty} d\xi \, f(\xi) \exp\left(-\frac{D}{\xi^2} n^2 \pi^2 t\right) \\ f(\xi) &= \frac{1}{\sqrt{2\pi\sigma^2}} \exp\left(-\frac{1}{2} \left(\frac{\xi - R}{\sigma}\right)^2\right) \end{split} \tag{2}$$

where σ is the standard deviation of sizes ξ . Regression of measured data to Eq. (2) gives estimates for the model's two independent parameters D/R^2 and σ . Table 2 lists the D/R^2 estimates obtained from non-linear regression of transient sorption data to either Eq. (1) or Eq. (2). These D/R^2 values are similar in magnitude, when scaled by the square of crystallite size, to those archived in the open literature for natural chabazite [67,68], aluminosilicate CHA [69], and SAPO-34 [70,71].

3.2. Effect of diffusional constraints on total turnovers in methanol-toolefins catalysis

Total turnovers of HSAPO-34 for methanol-to-olefins catalysis is defined as the methanol converted to hydrocarbon products appearing in the effluent throughout the lifetime of the catalyst per H^{\star} , i.e.,

total turnovers
$$\equiv \frac{1}{\mathcal{N}_{\mathrm{H}^{+}}^{\circ}} \int_{0}^{\tau_{\mathrm{d}}} dt \sum_{m} \sum_{n} m F_{\mathsf{C}_{m}\mathsf{H}_{n}}(t, z = \ell),$$
 (3)

where t is time-on-stream, τ_d is the time-on-stream when methanol conversion to effluent hydrocarbon products is zero, $\mathcal{N}_{H^+}^{\circ}$ is the moles of H^+ in the fixed-bed at t=0, and $F_{\mathsf{C}_m H_n}(t,z=\ell)$ is the molar

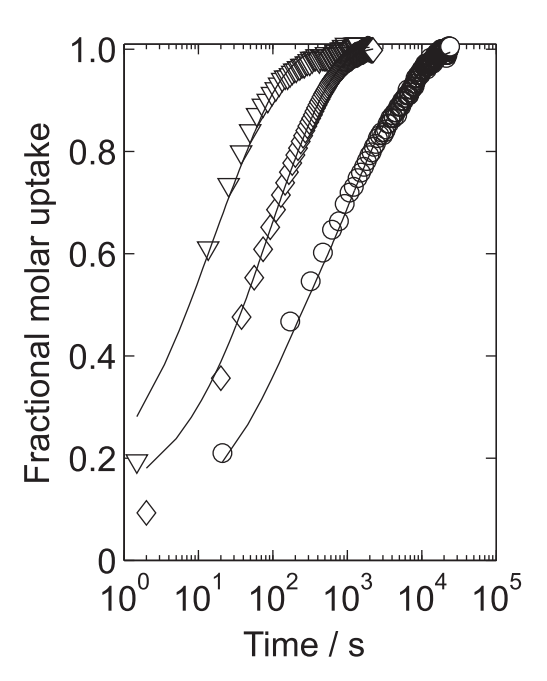


Fig. 2. Fractional molar uptake versus time during transient sorption of propane at 333 K on HSAPO-34 samples 1 (∇) , 6 (\Diamond) , and 9 (\circ) in Table 2. Solid lines represent curves obtained from non-linear regression of experimental data to Eqs. (1) and (2); the regressed D/R^2 values are listed in Table 2.

flow rate of C_mH_n at t in the fixed-bed effluent ($z=\ell$) [72]. The shape-selective properties of HSAPO-34—namely, the 3.8 Å pore openings [10]—restrict the distribution of hydrocarbons appearing in the fixed-bed effluent during methanol-to-olefins catalysis to C_1 – C_7 acyclic aliphatics [6]. Total turnovers provides an assessment of catalyst lifetime [18,72,73] that is intrinsic to the structural and chemical properties of the zeotype/zeolite formulation and to the methanol-to-olefins reaction conditions [18].

Total turnovers decreases monotonically with increasing values of $\rho_{\rm H^+}^{\circ}(R^2/D)$, where $\rho_{\rm H^+}^{\circ}$ and R^2/D are the H⁺ densities and size parameters, respectively, reported in Table 2. Methanol conversion to hydrocarbon products remains below 100% at all times-onstream for all samples at the selected reaction conditions (673 K, 16 kPa CH₃OH, 1700 MeOH $(H^+ \cdot ks)^{-1}$). The trend follows a smooth curve for samples with uniquely isolated Si speciation (Fig. 3, filled symbols). This trend is consistent with reported effects of crystallite size, site density, and textural properties on lifetime of CHA zeotypes and zeolites for methanol-to-olefins catalysis [14,20-27,29-32]. Total turnovers is smaller, at identical values of $\rho_{\text{\tiny H+}}^{\circ}(R^2/D)$, for samples exhibiting signals attributed to siliceous islands in ²⁹Si MAS NMR spectra (Fig. 3, open symbols) compared to those with uniquely Si(OAl)₄ speciation. This trend is consistent with reported effects of Si speciation on lifetime of HSAPO-34 for methanol-to-olefins catalysis [28]. The following mathematical treatment of reaction-transport phenomena in methanol-toolefins catalysis reveals that the effects of H⁺ density, crystallite size, and Si speciation on total turnovers are all manifestations of differences in diffusional constraints on methylation, hydrogen transfer, dealkylation, and dehydrocyclization rates.

Temporal and spatial concentration gradients persist at timeand length-scales spanning many decades during methanol-toolefins catalysis on HSAPO-34. These circumstances render impractical, if not impossible, the evaluation of instantaneous or steadystate rates of individual reactions and restrict analyses, and interpretations thereof, to rates averaged in both time and space. The

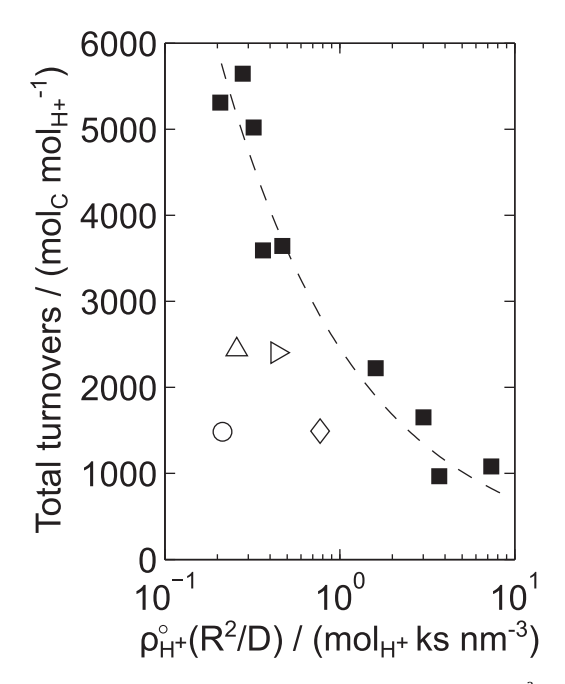


Fig. 3. Total turnovers for methanol-to-olefins catalysis versus $\rho_{\mathrm{H}^+}^{\circ}(R^2/D)$. Filled symbols denote samples with uniquely isolated Si, i.e., 100% Si(OAl)₄ Si speciation (samples 1–9 in Table 2), and open symbols denote samples with \leqslant 86% Si(OAl)₄ Si speciation (samples 10–13 in Table 2). Reaction conditions: 673 K, 16 kPa CH₃OH, 1700 MeOH (H $^+$ · ks $^{-1}$). The dashed line is a guide for the eye.

temporal and spatial evolution of the concentration of hydrocarbon C_mH_n is governed by material balance

$$\frac{\partial C_{C_m H_n}}{\partial t} + \nabla \cdot \mathbf{N}_{C_m H_n} = r_{C_m H_n}^{obs},$$

where $C_{C_mH_n}$ is the concentration of C_mH_n , $\mathbf{N}_{C_mH_n}$ is the molar flux of C_mH_n , and $r_{C_mH_n}^{\mathrm{obs}}$ is the observed volumetric rate of formation of C_mH_n [74]. For a uniaxial, tubular fixed-bed reactor, considering time- and length-scales similar in magnitude for bulk convective flux and chemical reaction, the material balance reduces to

$$\frac{1}{A_{v}}\frac{\partial F_{C_{m}H_{n}}}{\partial z} = r_{C_{m}H_{n}}^{obs} - \frac{\partial C_{C_{m}H_{n}}}{\partial t},$$

the typical design equation for a packed-bed reactor [75] where A_x is the cross-sectional area. The reactor is devoid of radial and angular concentration gradients and operates under conditions with constant velocity and with bulk diffusive flux time-scales much smaller than the time-scales for both convective flux and chemical reaction [75]. Integration of the material balance in space from the fixed-bed influent (z=0) to the fixed-bed effluent $(z=\ell)$ and in time from t=0 to $t=\tau_d$ gives the following relation

$$\int_{0}^{\tau_{\rm d}} dt \, F_{\mathsf{C}_m \mathsf{H}_n}(t, z = \ell) = \mathcal{V} \int_{0}^{\tau_{\rm d}} dt \, \langle r_{\mathsf{C}_m \mathsf{H}_n}^{\mathsf{obs}} \rangle, \tag{4}$$

where $\mathcal{V}=A_x\ell$ is the volume of the fixed-bed and $\langle f(t,z)\rangle$, e.g., is the spatial average of f(t,z), i.e., $\langle f(t,z)\rangle=\mathcal{F}(t)=\mathcal{Z}^{-1}\int_0^z dz f(t,z)$. The integration across the spatial domain applies the boundary condition stipulating that the molar flow rate of C_mH_n at z=0, the fixed-bed influent, is zero at all values of t. The integration across the temporal domain utilizes the initial and final conditions stipulating that the concentration of C_mH_n at both t=0 and $t=\tau_d$ is zero at all values of z. These boundary, initial, and final conditions arise because hydrocarbons (C_mH_n) are, by definition, products in methanol-to-olefins catalysis. Substitution of Eq. (4) into the definition of total turnovers (Eq. (3)) gives

total turnovers =
$$\frac{\mathcal{V}\tau_d}{\mathcal{N}_{\text{H}^+}^{\circ}} \left(\frac{1}{\tau_d} \int_0^{\tau_d} dt \sum_m \sum_n m \langle r_{\text{C}_m H_n}^{\text{obs}} \rangle \right).$$
 (5)

The observed volumetric rate of formation of C_mH_n is the sum of observed volumetric rates of all reactions within the complex reaction network for methanol-to-olefins catalysis weighted by the stoichiometric coefficients for C_mH_n , i.e.,

$$r_{\mathsf{C}_m\mathsf{H}_n}^{\mathsf{obs}} = \sum_p v_{\mathsf{C}_m\mathsf{H}_n,p} \, r_p^{\mathsf{obs}},\tag{6}$$

where $v_{C_mH_n,p}$ is the stoichiometric coefficient for C_mH_n in reaction p and r_p^{obs} is the observed volumetric rate of reaction p. r_p^{obs} is the product of the overall effectiveness factor, η_p , that accounts for concentration gradients at particle and crystallite length-scales, and the volumetric rate of reaction p under hypothetical conditions of flat concentration gradients at particle and crystallite length-scales, r_p , [76] i.e.,

$$r_{\mathsf{C}_m\mathsf{H}_n}^{\mathsf{obs}} = \sum_p v_{\mathsf{C}_m\mathsf{H}_n,p} \, \eta_p \, r_p.$$

The overall effectiveness factor is the quantitative assessment of diffusional constraints-increasing deviations from unity indicate increasing deviations from flat concentration profiles. The overall effectiveness factor is parameterized by reaction properties (e.g., rate constants), molecular transport properties (e.g., diffusion constants), and structural catalyst properties (e.g., site density and particle/crystallite size) [77,76]. It is experimentally inaccessible for reactions involved in and at conditions relevant to methanolto-olefins catalysis; access is contingent on either a priori measurement of an intrinsic reaction rate or a priori knowledge of the rate expression and quantification of rate parameters—both formidable tasks in complex reaction networks occurring within reactors with both temporal and spatial gradients. The archived literature includes, however, examples demonstrating virtue of a combined parameter, site density (e.g., ρ_{H^+}) multiplied to a size parameter (e.g., R^2/D), to assess diffusional constraints in, e.g., CO hydrogenation on Co catalysts [77], alkene coupling on solid acids [78], alkane hydroisomerization on metal-acid bifunctional formulations [79,80], and methanol-to-hydrocarbons catalysis on HZSM-5 [81].

This virtue is a consequence of the general functional relationship between effectiveness factor, site density, and particle/crystallite size [76–80,82]. The overall effectiveness factor is a conflation of effectiveness factors describing transport constraints imposed at disparate length-scales [76]. The effectiveness factor describing diffusional constraints at length-scales of crystallites is a function of Thiele modulus [83], ϕ_p^2 , which assesses the relative volumetric rate of reaction versus diffusion within an intracrystalline domain,

$$\begin{split} \phi_{p}^{2} &= \frac{(r_{p})_{s}}{(D_{\mathsf{C}_{m}\mathsf{H}_{n}}/R^{2}) (C_{\mathsf{C}_{m}\mathsf{H}_{n}})_{s}} \\ &= \left(\frac{\rho_{\mathsf{H}^{+}}}{\rho_{\mathsf{H}^{+}}^{\circ}}\right) \cdot \left(\rho_{\mathsf{H}^{+}}^{\circ}(R^{2}/D)\right) \cdot \left(\frac{(r_{p,\mathsf{H}^{+}})_{s}/(C_{\mathsf{C}_{m}\mathsf{H}_{n}})_{s}}{D_{\mathsf{C}_{m}\mathsf{H}_{n}}/D}\right) \end{split} \tag{7}$$

where $(r_p)_s, (r_{p,H^+})_s$, and $(C_{\mathsf{C}_m\mathsf{H}_n})_s$ are the rate of reaction p per volume, rate of reaction p per H^+ , and concentration of $\mathsf{C}_m\mathsf{H}_n$, respectively, evaluated at hypothetical conditions of flat concentration gradients at crystallite length-scales; ρ_{H^+} is the instantaneous H^+ density; and $D_{\mathsf{C}_m\mathsf{H}_n}$ is the effective diffusion constant of $\mathsf{C}_m\mathsf{H}_n$. ($\rho_{\mathsf{H}^+}^\circ$ is the H^+ density defined in Table 2, and D/R^2 is the size parameter defined in Table 2 and Section 3.1.3.) This effectiveness factor deviates further from unity with increasing values of Thiele modulus, in general, for isothermal systems and for reaction-transport phenomena conferring large diffusional constraints ($\phi_n^2\gg 1$) [76].

The applied segregation of terms in Eq. (7) elucidates factors affecting diffusional constraints imposed at length-scales of crystallites [77]. The first term $\rho_{\rm H^+}/\rho_{\rm H^+}^\circ$ accounts for H⁺ loss during catalyst deactivation; the effect of diffusional constraints on total turnovers is ultimately insensitive to this effect of catalyst deactivation on Thiele modulus because total turnovers is a quantity averaged in time throughout the catalyst lifetime (Eqs. (3) and (5)). The second term, $\rho_{\rm H^+}^\circ(R^2/D)$, contains structural catalyst properties, and the third term,

$$\psi \equiv [(r_{n,H^+})_c/(C_{C_mH_n})_s]/[D_{C_mH_n}/D], \tag{8}$$

contains intrinsic kinetic constants (normalized per H⁺) and diffusion parameters. The effects of site density, crystallite size, and Si speciation on total turnovers (Fig. 3) are manifestations of effects of structural catalyst properties and intrinsic kinetic constants on the observed rates of formation of hydrocarbons appearing in the fixed-bed effluent.

Diffusional constraints increase with increasing values of $\rho_{\rm H^+}^{\circ}(R^2/D)$. Total turnovers decreases monotonically with increasing diffusional constraints, as modulated by $ho_{
m H^+}^{\circ}(R^2/D)$, for HSAPO-34 samples with uniquely Si(OAl)₄ speciation (closed symbols in Fig. 3). The monotonic trend conforms with the single-site nature of such materials [35,84], and the single-site nature implies uniformity in ψ values (Eq. (8)) regardless of $\rho_{H^+}^{\circ}(R^2/D)$ values because rates per H⁺ and effective diffusion constants are properties intrinsic to the single-site and CHA topology. Total turnovers is smaller, at identical $\rho_{\mathrm{H^+}}^{\circ}(R^2/D)$ values, for HSAPO-34 samples with siliceous islands (open symbols in Fig. 3) compared to HSAPO-34 samples with uniquely isolated Si(OAl)₄ speciation (closed symbols in Fig. 3). This implies that the presence of siliceous islands increases diffusional constraints via increases in ψ values. The topology is CHA regardless of Si speciation so siliceous islands must affect ψ values by changes to intrinsic kinetic constants. This effect of Si speciation is consistent with site heterogeneity of silicoaluminophosphates diverse in Si speciation and is likely a consequence of increased acid strength for protons attendant to siliceous islands compared to protons attendant to isolated Si [33,35,48-50]. Further analysis of the trend for single-site HSAPO-34 samples in Fig. 3 within the context of this reactiontransport formalism, together with consideration of the complex reaction network for methanol-to-olefins catalysis, enables insight, however modest, on the relative effects of diffusional constraints on rates of specific reaction classes.

The defintion of total turnovers includes a summation of species (m, n) and reactions (p); substitution of Eq. (6) into Eq. (5) gives

$$\text{total turnovers} = \frac{\mathcal{V}\tau_d}{\mathcal{N}_{\mathrm{H}^+}^{\circ}} \left(\frac{1}{\tau_d} \int_0^{\tau_d} dt \underset{m}{\sum} \underset{n}{\sum} \underset{p}{\sum} m \, v_{\mathsf{C}_m \mathsf{H}_n, p} \, \langle r_p^{\mathsf{obs}} \rangle \right),$$

and the monotonically decreasing trend of total turnovers with $\rho_{\rm H^+}^\circ(R^2/D)$ (Fig. 3) prescribes the following inequality:

$$\frac{\partial}{\partial \left(\rho_{\mathrm{H}^{+}}^{\circ}(R^{2}/D)\right)} \left(\int_{0}^{\tau_{\mathrm{d}}} dt \sum_{m} \sum_{n} \sum_{p} m v_{\mathsf{C}_{m}\mathsf{H}_{n},p} \left\langle r_{p}^{\mathrm{obs}} \right\rangle \right) < 0. \tag{9}$$

The reactions within the complex reaction network for methanol-to-olefins catalysis with non-zero $v_{C_m H_n, p}$ comprise methylation, oligomerization, β -scission, dealkylation, hydrogen transfer, and dehydrocyclization [8], and the hydrocarbon products detected in the fixed-bed effluent comprise C_1 to C_7 acyclic aliphatics. Rates of oligomerization, β -scission, and hydrogen transfer between acyclic aliphatics cancel, ultimately, in the m-weighted sum over all effluent hydrocarbon products (sums with indices m

and n) and the $v_{C_mH_n,p}$ -weighted sum over all reactions (sum with index p) in Eq. (9). Consider, e.g., the oligomerization of C_aH_c with C_bH_d ,

$$C_aH_c + C_bH_d \stackrel{p^*}{\rightarrow} C_{a+b}H_{c+d}$$
.

The observed rate of consumption of C_aH_c and C_bH_d via oligomerization is canceled exactly by the rate of formation of oligomer $C_{a+b}H_{c+d}$ via the identical reaction, i.e.,

$$\sum_{m}\sum_{n}mv_{\mathsf{C}_{m}\mathsf{H}_{n},p^{*}}r_{p^{*}}^{\mathsf{obs}}=[a(-1)+b(-1)+(a+b)(1)]r_{p^{*}}^{\mathsf{obs}}=0$$

The rates of consumption of reactants and rates of formation of products in β -scission reactions cancel exactly in the reverse fashion as oligomerization. Consider also hydrogen transfer between C_a - H_c and C_bH_d ; the observed rate of consumption of C_aH_c and C_bH_d via hydrogen transfer is canceled exactly by the rate of formation of $C_aH_{c\pm 2}$ and $C_bH_{d\mp 2}$ via the identical reaction. Only olefins methylation, aromatics dealkylation, methanol transfer hydrogenation, and olefins dehydrocyclization contribute, ultimately, to the triple summation in Eq. (9).

The cascade of olefins methylation results ultimately in the net formation of an effluent hydrocarbon; aromatics dealkylation results ultimately in the net formation of an effluent hydrocarbon; methanol transfer hydrogenation results in the net formation methane; and, dehydrocyclization results ultimately in the net consumption of a hydrocarbon. Manipulation of the inequality in Eq. (9) to distinguish reactions with $v_{C_mH_n,p} > 0$ from those with $v_{C_mH_n,p} < 0$ gives

$$\int_{0}^{\tau_{d}} dt \sum_{m} \sum_{n} \sum_{p} m |\nu_{C_{m}H_{n},p}| \left\langle \frac{\partial r_{p}^{\text{obs}}}{\partial \left(\rho_{H^{+}}^{\circ}(R^{2}/D)\right)} \right\rangle \\
< \int_{0}^{\tau_{d}} dt \sum_{m} \sum_{n} \sum_{p} m |\nu_{C_{m}H_{n},p}| \left\langle \frac{\partial r_{p}^{\text{obs}}}{\partial \left(\rho_{H^{+}}^{\circ}(R^{2}/D)\right)} \right\rangle.$$
(10)

The left-hand side of the inequality in Eq. (10) includes only the observed rate of the methylation cascade, methanol transfer hydrogenation, and aromatics dealkylation, and the right-hand side includes only the observed rates of dehydrocyclization. Alternatively, the left-hand side includes only the rates of reactions that ultimately consume methanol to give an effluent hydrocarbon product, and the right-hand side includes only the rates of reactions that ultimately consume methanol to give or augment an entrained hydrocarbon. The inequality in Eq. (10) states that observed rates of productive reactions decrease more with increasing diffusional constraints imposed by the structural catalyst properties than observed rates of nonproductive reactions. More specifically, rates of dehydrocyclization are less sensitive, onaverage, to diffusional constraints than rates of methylation, methanol transfer hydrogenation, and aromatics dealkylation.

The aliphatic precursors to aromatics in solid-acid mediated dehydrocyclization include acyclic and cyclic hydrocarbons of varying degrees of unsaturation [85–88]. Only acyclic species are detected in the fixed-bed effluent in methanol-to-olefins catalysis, and only these are enumerated in the summations indices to evaluate total turnovers (Eq. (3)). Backbone chain-lengths of acyclic aliphatic precursors for aromatization are necessarily larger than or equal to six. The inequality in Eq. (10) suggests then that the intrinsic kinetic properties, i.e., rate constants per H $^+$, and topological features, i.e., eight-membered ring apertures, of HSAPO-34 confer such strong diffusional constraints on C $_{6+}$ aromatization precursors that variations in structural catalyst properties, i.e., site density and crystallite size, confer only minimal effect on observed rates of dehydrocyclization. The diffusional constraints imposed by

intrinsic kinetic properties and topological features of HSAPO-34 on gas-phase reactants in the methylation cascade (C_2 - C_6 olefins, methanol, and dimethyl ether), methanol transfer hydrogenation (aliphatic hydrocarbons and methanol), and aromatics dealkylation (methanol and dimethyl ether) are on average less severe than those imposed on C₆₊ aromatization precursors such that variations in structural catalyst properties confer profound effects on diffusional constraints for these reactions. (Effectiveness factor scales as the inverse of Thiele modulus. The sensitivity of effectiveness factor with Thiele modulus scales then as the inverse-square of Thiele modulus.) This implies that the effective diffusion constants for C₆₊ aromatization precursors are so small that the orders-of-magnitude variations in $\rho_{\rm H^+}^{\circ}(R^2/D)$ affect the effectiveness factors for aromatization less, on-average, than effectiveness factors for methylation, methanol transfer hydrogenation, and aromatics dealkylation because the effective diffusion constants for gas-phase reactants of these reactions (methanol, dimethyl ether, and aliphatics) are comparatively large. Alternatively, this implies that the average intrinsic rates per H⁺ for dehydrocyclization are so large that the orders-of-magnitude variations in $\rho_{\rm H^+}^{\circ}(R^2/D)$ affect the effectiveness factors for aromatization less, on-average, than effectiveness factors for methylation, methanol transfer hydrogenation, and aromatics dealkylation because the average intrinsic rates per H⁺ for gas-phase reactants of these reactions are comparatively small. Succinctly, the trend in Fig. 3 (and inequality in Eq. (10)) implies that the Thiele moduli for dehydrocyclization is larger, on-average, than the Thiele moduli for methylation, methanol transfer hydrogenation, and aromatics dealkylation.

3.3. Effect of diffusional constraints on cumulative selectivity in methanol-to-olefins catalysis

The coupled temporal and spatial gradients rendering impractical the evaluation of instanteous and steady-state rates in methanol-to-olefins catalysis prevail also to preclude precise kinetic and mechanistic interpretation of instantaneous selectivity data. The utility of the reaction-transport formalism detailed in Section 3.2 to reveal effects of diffusional constraints on reaction rates averaged in time and space extends to the analysis of selectivity averaged in time and space. The cumulative selectivity to effluent hydrocarbon product C_mH_n ($\mathcal{S}_{C_mH_n}$) is defined [18,73] as

$$\mathcal{S}_{\mathsf{C}_{m}\mathsf{H}_{n}} \equiv \frac{\int_{0}^{\tau_{d}} dt \, m F_{\mathsf{C}_{m}\mathsf{H}_{n}}(t, z = \ell)}{\int_{0}^{\tau_{d}} dt \sum_{m'} \sum_{n'} m' F_{\mathsf{C}_{m'}\mathsf{H}_{n'}}(t, z = \ell)}$$

$$= \frac{\frac{1}{\tau_{d}} \int_{0}^{\tau_{d}} dt \sum_{p} m \, v_{\mathsf{C}_{m}\mathsf{H}_{n}, p} \, \langle r_{p}^{\mathsf{obs}} \rangle}{\frac{1}{\tau_{d}} \int_{0}^{\tau_{d}} dt \sum_{m'} \sum_{n'} \sum_{p'} m' \, v_{\mathsf{C}_{m'}\mathsf{H}_{n'}, p'} \, \langle r_{p'}^{\mathsf{obs}} \rangle}$$

$$= \frac{\frac{\mathcal{V}_{\tau_{d}}}{N_{\mathsf{H}^{+}}^{\mathsf{c}}} \left(\frac{1}{\tau_{d}} \int_{0}^{\tau_{d}} dt \sum_{p} m \, v_{\mathsf{C}_{m}\mathsf{H}_{n}, p} \, \langle r_{p}^{\mathsf{obs}} \rangle \right)}{\mathsf{total} \, \mathsf{turnovers}}. \tag{12}$$

 $S_{C_m H_n}$ is the ratio of the time- and space-averaged net rate of formation of $C_m H_n$ to the time- and space-averaged rates of the methylation cascade, methanol transfer hydrogenation, aromatics dealkylation, and dehydrocyclization (Eq. (11)). Equivalently, $S_{C_m H_n}$ is the fractional contribution of total turnovers from $C_m H_n$ (Eq. (12)).

Fig. 4a shows that the cumulative selectivities to ethylene, propylene, butenes, and C_5 and C_{6+} acyclic aliphatics are largely invariant with $\rho_{\rm H^+}^\circ(R^2/D)$ for samples 1–9 in Table 2. These invariances imply that the sensitivity of time- and space-averaged net rates of ethylene, propylene, butenes, C_5 , and C_{6+} formation to diffusional constraints conferred by structural catalyst properties are similar to that for the time- and space-averaged rates of the methylation cascade, methanol transfer hydrogenation, aromatics dealkylation, and dehydrocyclization. This suggests that ethylene, propylene, butenes, and C_{5+} acyclic aliphatics share, on average,

identical kinetic origin with the possibilites limited to the methylation cascade, methanol transfer hydrogenation, aromatics dealkylation, and dehydrocyclization. Methanol transfer hydrogenation and dehydrocyclization are eliminated because these reactions ultimately consume an olefin, and the methylation cascade is eliminated because ethylene is not a product of methylation [72,89–91]. Thus, the invariances in olefins cumulative selectivities with $\rho_{\rm in}^*(R^2/D)$ (Fig. 4a) suggest that the kinetically-dominant pathway for formation of all olefins products when averaged throughout the catalyst lifetime and across the fixed-bed is aromatics dealkylation. This result is consistent with aromatics comprising the pool of organic co-catalysts throughout the majority of turnovers in methanol-to-olefins catalysis [11,12,24].

The cumulative selectivities to methane, ethane, and propane increase with increasing $\rho_{\rm H^+}^{\circ}(R^2/D)$ (Fig. 4b) while the cumulative selectivity to butanes is invariant with $\rho_{\rm H^+}^{\circ}(R^2/D)$. These trends translate into the following inequalities

$$0 < \frac{\partial \mathcal{S}_{\mathsf{C}_{\mathsf{n}}\mathsf{H}_{2n+2}}}{\partial \left(\rho_{\mathsf{H}^{+}}^{\circ}(R^{2}/D)\right)}$$

$$= \frac{\partial}{\partial \left(\rho_{\mathsf{H}^{+}}^{\circ}(R^{2}/D)\right)} \left(\frac{\frac{1}{\tau_{d}} \int_{0}^{\tau_{d}} dt \sum_{p} n \, \nu_{\mathsf{C}_{\mathsf{n}}\mathsf{H}_{2n+2},p} \, \langle r_{p}^{\mathsf{obs}} \rangle}{\frac{1}{\tau_{d}} \int_{0}^{\tau_{d}} dt \sum_{m'} \sum_{n'} \sum_{p'} m' \, \nu_{\mathsf{C}_{m'}\mathsf{H}_{n'},p'} \, \langle r_{p'}^{\mathsf{obs}} \rangle}\right) \tag{13}$$

for $n=1,\,2$, and 3. Applying the quotient rule for differentiation to Eq. (13) and assuming the inequality $(\partial \langle r_p^{\rm obs} \rangle / \partial \left(\rho_{\rm H^+}^{\circ}(R^2/D) \right)) < 0-$ i.e., observed rates decrease with increasing diffusional constraints imposed by structural catalyst properties (rigorously true for isothermal systems and reactions with strong diffusional limitations $(\phi \gg 1)$)—gives

$$\begin{split} &\frac{\frac{1}{\tau_d}\int_0^{\tau_d}dt\sum_{m'}\sum_{n'}\sum_{p'}m'\,\nu_{\mathsf{C}_{m'}\mathsf{H}_{n'},p'}\left|\frac{\partial\langle r_{p'}^{\mathsf{obs}}\rangle}{\partial\left(\rho_{\mathsf{H}^+}^{\mathsf{c}}(\mathsf{R}^2/D)\right)}\right|}{\frac{\frac{1}{\tau_d}\int_0^{\tau_d}dt\sum_{p}n\,\nu_{\mathsf{C}_n\mathsf{H}_{2n+2},p}\left|\frac{\partial\langle r_{p'}^{\mathsf{obs}}\rangle}{\partial\left(\rho_{\mathsf{H}^+}^{\mathsf{c}}(\mathsf{R}^2/D)\right)}\right|}\\ &>\frac{\frac{1}{\tau_d}\int_0^{\tau_d}dt\sum_{m'}\sum_{n'}\sum_{p'}m'\,\nu_{\mathsf{C}_{m'}\mathsf{H}_{n'},p'}\left\langle r_{p'}^{\mathsf{obs}}\right\rangle}{\frac{1}{\tau_d}\int_0^{\tau_d}dt\sum_{p}n\,\nu_{\mathsf{C}_n\mathsf{H}_{2n+2},p}\left\langle r_{p'}^{\mathsf{obs}}\right\rangle}, \end{split}$$

and applying the definition in Eq. (11) and the inequality $S_{C_mH_\eta} < 1$, i.e., the cumulative selectivity to any effluent hydrocarbon is less than 100%, gives

$$\frac{1}{\tau_{d}} \int_{0}^{\tau_{d}} dt \sum_{m'} \sum_{n'} \sum_{p'} m' v_{C_{m'}H_{n'},p'} \left| \frac{\partial \langle r_{p'}^{\text{obs}} \rangle}{\partial \left(\rho_{H^{+}}^{\circ}(R^{2}/D) \right)} \right|
> \frac{1}{\tau_{d}} \int_{0}^{\tau_{d}} dt \sum_{p} n v_{C_{n}H_{2n+2},p} \left| \frac{\partial \langle r_{p}^{\text{obs}} \rangle}{\partial \left(\rho_{H^{+}}^{\circ}(R^{2}/D) \right)} \right|.$$
(14)

The left-hand side of the inequality in Eq. (14) includes only, as discussed in Section 3.2, the observed rates of the methylation cascade, methanol transfer hydrogenation, aromatics dealkylation, and dehydrocyclization. The right-hand side includes the rates of reactions producing and consuming methane, ethane, and propane (n=1, 2, and 3, respectively). Methane, ethane, and propane are produced in transfer hydrogenation of methanol, ethylene, and propylene, respectively, and ethane and propane are consumed in transfer dehydrogenation. The inequality in Eq. (14) then implies that the net rates of hydrogen transfer reactions involving C_1 – C_3 species are less sensitive to diffusional constraints than the rates of the methylation cascade, methanol transfer hydrogenation, aromatics dealkylation, and dehydrocyclization. This implies that the Thiele moduli for transfer hydrogenation reactions of methanol,

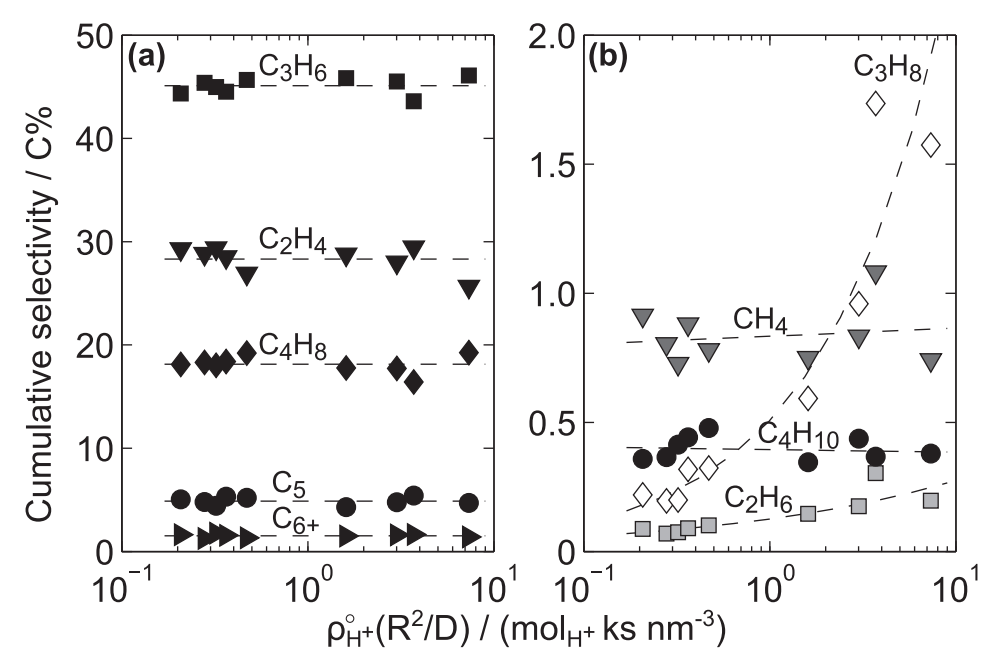


Fig. 4. Cumulative selectivity of (a) C_2H_4 , C_3H_6 , C_4H_8 , C_5 acyclic aliphatics, and C_{6+} acyclic aliphatics and (b) CH_4 , C_2H_6 , C_3H_8 , and C_4H_{10} in methanol-to-olefins catalysis versus $\rho_{1+}^{\circ}(R^2/D)$ for HSAPO-34 samples 1–9 in Table 2. Reaction conditions: 673 K, 16 kPa CH_3OH , 1700 MeOH $(H^+ \cdot ks^{-1})$. The dashed lines are guides for the eye.

ethylene, and propylene are larger, on-average, than the Thiele moduli for methylation, methanol transfer hydrogenation, aromatics dealkylation, and dehydrocyclization. This result is consistent with the results in Section 3.2—Thiele moduli for dehydrocyclization are larger, on-average, than the Thiele moduli for methylation, methanol transfer hydrogenation, and aromatics dealkylation—because methane, ethane, and propane are the hydrogen-rich byproducts formed along the dehydrocyclization cascade.

4. Conclusions

The effects of crystallite size, H⁺ density, and Si speciation of HSAPO-34 on catalyst lifetime and selectivity in methanol-toolefins catalysis are all manifestations of diffusional constraints. Diffusional constraints increase with increasing values of a combined parameter of structural catalyst properties—H⁺ density multiplied to a functional assessment of crystallite size $(\rho_{H^+}^{\circ}(R^2/D))$. Diffusional constraints are also sensitive to Si speciation because the local coordinative environment of the heteroatom affects, apparently, the intrinsic kinetic constants. Rigorous assessment of the effects of diffusional constraints on rates of reactions within the complex reaction network for methanol-to-olefins catalysis requires quantities derived from observables that avoid conflation by temporal and spatial gradients. Total turnovers is the sum of hydrocarbon formation rates averaged in space, across the fixedbed, and in time, throughout the catalyst lifetime; total turnovers is an intensive assessment of catalyst lifetime in methanol-toolefins catalysis on HSAPO-34. Total turnovers decreases with increasing diffusional constraints regulated either by $\rho_{\mu+}^{\circ}(R^2/D)$ or by Si speciation. Reaction-transport analysis of the complex reaction network for methanol-to-olefins catalysis shows that the effect of diffusional constraints on total turnovers arises because dehydrocyclization reactions experience stronger diffusional constraints than olefins methylation, methanol transfer hydrogenation, and aromatics dealkylation. Cumulative selectivity to a given hydrocarbon product, C_mH_n , is the space- and timeaveraged rate of formation of C_mH_n normalized by the sum of space- and time-averaged rates of formation of all hydrocarbon products. Cumulative selectivities to methane, ethane, and propane increase with increasing diffusional constraints demonstrating that transfer hydrogenation of methanol, ethylene, and propylene experience stronger diffusional constraints than all other reactions within the complex reaction network. The methodology and results reported here represent a case-study for the analysis of reaction-transport phenomena occurring within complex reaction networks in heterogeneous catalysis where both temporal and spatial concentration gradients prevail.

Acknowledgments

We acknowledge Dr. Tanya Whitmer (Ohio State University) for acquiring MAS NMR spectra. AH, ZS, and AB acknowledge financial support from the Dow Chemical Company and the National Science Foundation (CBET 1701534). JDR acknowledges financial support from the U.S. Department of Energy, Office of Basic Energy Sciences (DESC0014468).

Appendix A. Supplementary data

Supplementary data associated with this article can be found, in the online version, at https://doi.org/10.1016/j.jcat.2018.10.031.

References

- [1] N. Barkai, S. Leibler, Robustness in simple biochemical networks, Nature 387 (1997) 913–917.
- [2] T.P. Snow, V.M. Bierbaum, Ion chemistry in the interstellar medium, Annu. Rev. Anal. Chem. 1 (2008) 229–259.
- [3] R.G. Susnow, A.M. Dean, W.H. Green, P. Peczak, L.J. Broadbelt, Rate-based construction of kinetic models for complex systems, J. Phys. Chem. A 101 (1997) 3731–3740.
- [4] G.F. Froment, The kinetics of complex catalytic reactions, Chem. Eng. Sci 42 (1987) 1073–1087.
- [5] J.F. Haw, W. Song, D.M. Marcus, J.B. Nicholas, The mechanism of methanol to hydrocarbon catalysis, Acc. Chem. Res. 36 (2003) 317–326.
- [6] U. Olsbye, S. Svelle, M. Bjørgen, P. Beato, T.V.W. Janssens, F. Joensen, S. Bordiga, K.-P. Lillerud, Conversion of methanol to hydrocarbons: How zeolite cavity and pore size controls product selectivity, Angew. Chem. Int. Ed. 51 (2012) 5810– 5831.
- [7] S. Xu, Y. Zhi, J. Han, W. Zhang, X. Wu, T. Sun, Y. Wei, Z. Liu, Advances in catalysis for methanol-to-olefins conversion, Adv. Catal. 61 (2017) 37–122.

- [8] S. Ilias, A. Bhan, Mechanism of the catalytic conversion of methanol to hydrocarbons, ACS Catal. 3 (2013) 18–31.
- [9] B.M. Lok, C.A. Messina, R.L. Patton, R.T. Gajek, T.R. Cannan, E.M. Flanigen, Silicoaluminophosphate molecular sieves: Another new class of microporous crystalline inorganic solids, J. Am. Chem. Soc. 106 (1984) 6092–6093.
- [10] C. Baerlocher, L.B. McCusker, D.H. Olson, Atlas of Zeolite Framework Types, 6th ed., Elsevier, 2007.
- [11] W. Song, J.F. Haw, J.B. Nicholas, C.S. Heneghan, Methylbenzenes are the organic reaction centers for methanol-to-olefin catalysis on HSAPO-34, J. Am. Chem. Soc. 122 (2000) 10726–10727.
- [12] B. Arstad, S. Kolboe, The reactivity of molecules trapped within the SAPO-34 cavities in the methanol-to-hydrocarbons reaction, J. Am. Chem. Soc. 123 (2001) 8137–8138.
- [13] C.D. Chang, Hydrocarbons from methanol, Catal. Rev. Sci. Eng. 25 (1983) 1-
- [14] S. Wilson, P. Barger, The characteristics of SAPO-34 which influence the conversion of methanol to light olefins, Micropor. Mesopor. Mater. 29 (1999) 117–126.
- [15] P. Tian, Y. Wei, M. Ye, Z. Liu, Methanol to olefins (MTO): From fundamentals to commercialization, ACS Catal. 5 (2015) 1922–1938.
- [16] S. Müller, Y. Liu, M. Vishnuvarthan, X. Sun, A.C. van Veen, G.L. Haller, M. Sanchez-Sanchez, J.A. Lercher, Coke formation and deactivation pathways on H-ZSM-5 in the conversion of methanol to olefins, J. Catal. 325 (2015) 48–59.
- [17] S. Müller, Y. Liu, F.M. Kirchberger, M. Tonigold, M. Sanchez-Sanchez, J.A. Lercher, Hydrogen transfer pathways during zeolite catalyzed methanol conversion to hydrocarbons, J. Am. Chem. Soc 138 (2016) 15994–16003.
- [18] A. Hwang, M. Kumar, J.D. Rimer, A. Bhan, Implications of methanol disproportionation on catalyst lifetime for methanol-to-olefins conversion by HSSZ-13, J. Catal. 346 (2017) 154–160.
- [19] S.S. Arora, A. Bhan, The critical role of methanol pressure in controlling its transfer dehydrogenation and the corresponding effect on propylene-toethylene ratio during methanol-to-hydrocarbons catalysis on H-ZSM-5, J. Catal. 356 (2017) 300–306.
- [20] L.-T. Yuen, S.I. Zones, T.V. Harris, E.J. Gallegos, A. Auroux, Product selectivity in methanol to hydrocarbon conversion for isostructural compositions of AFI and CHA molecular sieves, Micropor. Mater. 2 (1994) 105–117.
- [21] I.M. Dahl, H. Mostad, D. Akporiaye, R. Wendelbo, Structural and chemical influences on the MTO reaction: A comparison of chabazite and SAPO-34 as MTO catalysts, Micropor. Mesopor. Mater. 29 (1999) 185–190.
- [22] D. Chen, K. Moljord, T. Fuglerud, A. Holmen, The effect of crystal size of SAPO-34 on the selectivity and deactivation of the MTO reaction, Micropor. Mesopor. Mater. 29 (1999) 191–203.
- [23] Q. Zhu, J.N. Kondo, R. Ohnuma, Y. Kubota, M. Yamaguchi, T. Tatsumi, The study of methanol-to-olefin over proton type aluminosilicate CHA zeolites, Micropor. Mesopor. Mater. 112 (2008) 153–161.
- [24] B.P.C. Hereijgers, F. Bleken, M.H. Nilsen, S. Svelle, K.-P. Lillerud, M. Bjørgen, B. M. Weckhuysen, U. Olsbye, Product shape selectivity dominates the methanol-to-olefins (MTO) reaction over H-SAPO-34 catalysts, J. Catal. 264 (2009) 77-87
- [25] W. Dai, X. Wang, G. Wu, L. Li, N. Guan, M. Hunger, Methanol-to-olefin conversion catalyzed by low-silica AIPO-34 with traces of Brønsted acid sites: Combined catalytic and spectroscopic investigations, ChemCatChem 4 (2012) 1428–1435.
- [26] P. Wang, A. Lv, J. Hu, J. Xu, G. Lu, The synthesis of SAPO-34 with mixed template and its catalytic performance for methanol to olefins reaction, Micropor. Mesopor. Mater. 152 (2012) 178–184.
- [27] W. Dai, G. Wu, L. Li, N. Guan, M. Hunger, Mechanisms of the deactivation of SAPO-34 materials with different crystal sizes applied as MTO catalysts, ACS Catal. 3 (2013) 588-596.
- [28] Z. Li, J. Martínez-Triguero, P. Concepción, J. Yu, A. Corma, Methanol to olefins: Activity and stability of nanosized SAPO-34 molecular sieves and control of selectivity by silicon distribution, Phys. Chem. Chem. Phys. 15 (2013) 14670– 14680
- [29] G. Yang, Y. Wei, S. Xu, J. Chen, J. Li, Z. Liu, J. Yu, R. Xu, Nanosize-enhanced lifetime of SAPO-34 catalysts in methanol-to-olefin reactions, J. Phys. Chem. C 117 (2013) 8214–8222.
- [30] M.A. Deimund, L. Harrison, J.D. Lunn, Y. Liu, A. Malek, R. Shayib, M.E. Davis, Effect of heteroatom concentration in SSZ-13 on the methanol-to-olefins reaction, ACS Catal. 6 (2016) 542–550.
- [31] X. Zhu, J.P. Hofmann, B. Mezari, N. Kosinov, L. Wu, Q. Qian, B.M. Weckhuysen, S. Asahina, J. Ruiz-Martínez, E.J.M. Hensen, Trimodal porous hierarchical SSZ-13 zeolite with improved catalytic performance in the methanol-to-olefins reaction, ACS Catal. 6 (2016) 2163–2177.
- [32] W. Dai, G. Cao, L. Yang, G. Wu, M. Dyballa, M. Hunger, N. Guan, L. Li, Insights into the catalytic cycle and activity of methanol-to-olefin conversion over low-silica AlPO-34 zeolites with controllable Brønsted acid density, Catal. Sci. Technol. 7 (2017) 607–618.
- [33] G. Sastre, D.W. Lewis, R.A. Catlow, Modeling of silicon substitution in SAPO-5 and SAPO-34 molecular sieves, J. Phys. Chem. B 101 (1997) 5249–5262.
- [34] L. Xu, A. Du, Y. Wei, Y. Wang, Z. Yu, Y. He, X. Zhang, Z. Liu, Synthesis of SAPO-34 with only Si(4Al) species: Effect of Si contents on Si incorporation mechanism and Si coordination environment of SAPO-34, Micropor. Mesopor. Mater. 115 (2008) 332–337.
- [35] D. Barthomeuf, Topological model for the compared acidity of SAPOs and SiAl zeolites, Zeolites 14 (1994) 394–401.

- [36] J. Tan, Z. Liu, X. Bao, X. Liu, X. Han, C. He, R. Zhai, Crystallization and Si incorporation mechanisms of SAPO-34, Micropor. Mesopor. Mater. 53 (2002) 97-108
- [37] H.J. Kim, J.-W. Kim, N. Kim, T.-W. Kim, S.H. Jhung, C.-U. Kim, Controlling size and acidity of SAPO-34 catalyst for efficient ethylene to propylene transformation, Mol. Catal. 438 (2017) 86–92.
- [38] H.-J. Chae, I.-J. Park, Y.-H. Song, K.-E. Jeong, C.-U. Kim, C.-H. Shin, S.-Y. Jeong, Physicochemical characteristics of SAPO-34 molecular sieves synthesized with mixed templates as MTO catalysts, J. Nanosci. Nanotechnol. 10 (2010) 195– 202
- [39] M. Ghavipour, A.S. Mehr, Y. Wang, R.M. Behbahani, S. Hajimirzaee, K. Bahrami, Investigating the mixing sequence and the Si content in SAPO-34 synthesis for selective conversion of methanol to light olefins using morpholine and TEAOH templates, RSC Adv. 6 (2016) 17583–17594.
- [40] L. Wu, Z. Liu, L. Xia, M. Qiu, X. Liu, H. Zhu, Y. Sun, Effect of SAPO-34 molecular sieve morphology on methanol to olefins performance, Chin. J. Catal. 34 (2013) 1348–1356.
- [41] X. Liu, S. Ren, G. Zeng, G. Liu, P. Wu, G. Wang, X. Chen, Z. Liu, Y. Sun, Coke suppression in MTO over hierarchical SAPO-34 zeolites, RSC Adv. 6 (2016) 28787–28791.
- [42] H. van Heyden, S. Mintova, T. Bein, Nanosized SAPO-34 synthesized from colloidal solutions, Chem. Mater. 20 (2008) 2956–2963.
- [43] R. Vomscheid, M. Briend, M.J. Peltre, P. Massiani, P.P. Man, D. Barthomeuf, Reversible modification of the Si environment in template-free SAPO-34 structure upon hydration-dehydration cycles below ca. 400 K, J. Chem. Soc. Chem. Comm. (1993) 544–546.
- [44] M.M.J. Treacy, J.B. Higgins (Eds.), Collection of Simulated XRD Powder Patterns for Zeolites, 4th ed., Elsevier, 2001.
- [45] B.C. Lippens, J.G. de Boer, Studies on pore systems in catalysts: V. the *t* method, I. Catal. 4 (1965) 319–323.
- [46] S.A. Bates, W.N. Delgass, F.H. Ribeiro, J.T. Miller, R. Gounder, Methods for NH₃ titration of Brønsted acid sites in Cu-zeolites that catalyze the selective catalytic reduction of NO₂ with NH₂. J. Catal. 312 (2014) 26–36.
- catalytic reduction of NO_x with NH₃, J. Catal. 312 (2014) 26–36.

 [47] E.M. Flanigen, R.L. Patton, S.T. Wilson, Structural, synthetic and physicochemical concepts in aluminophosphate-based molecular sieves, Stud. Surf. Sci. Catal. 37 (1988) 13–27.
- [48] G. Sastre, D.W. Lewis, Modelling of Brønsted acidity in AFI and CHA zeotypes, J. Chem. Soc., Faraday Trans. 94 (1998) 3049–3058.
- [49] J.A. Martens, P.J. Grobet, P.A. Jacobs, Catalytic activity and Si, Al, P ordering in microporous silicoaluminophosphates of the SAPO-5, SAPO-11, and SAPO-37 type, J. Catal. 126 (1990) 299–305.
- [50] G.A.V. Martins, G. Berlier, S. Coluccia, H.O. Pastore, G.B. Superti, G. Gatti, L. Marchese, Revisiting the nature of the acidity in chabazite-related silicoaluminophosphates: Combined FTIR and ²⁹Si MAS NMR study, J. Phys. Chem. C 111 (2007) 330–339.
- [51] R. Vomscheid, M. Briend, M.J. Peltre, P.P. Man, D. Barthomeuf, The role of the template in directing the Si distribution in SAPO zeolites, J. Phys. Chem. 98 (1994) 9614–9618.
- [52] A. Buchholz, W. Wang, M. Xu, A. Arnold, M. Hunger, Thermal stability and dehydroxylation of Brønsted acid sites in silicoaluminophosphates H-SAPO-11, H-SAPO-18, H-SAPO-31, and H-SAPO-34 investigated by multi-nuclear solid-state NMR spectroscopy, Micropor. Mesopor. Mater. 56 (2002) 267–278.
- [53] L.R. Aramburo, J. Ruiz-Martínez, L. Sommer, B. Arstad, R. Buitrago-Sierra, A. Sepúlveda-Escribano, H.W. Zandbergen, U. Olsbye, F.M.F. de Groot, B.M. Weckhuysen, X-ray imaging of SAPO-34 molecular sieves at the nanoscale: Influence of steaming on the methanol-to-hydrocarbons reaction, ChemCatChem 5 (2013) 1386–1394.
- [54] A. Buchholz, W. Wang, A. Arnold, M. Xu, M. Hunger, Successive steps of hydration and dehydration of silicoaluminophosphates H-SAPO-34 and H-SAPO-37 investigated by in situ CF MAS NMR spectroscopy, Micropor. Mesopor. Mater. 57 (2003) 157–168.
- [55] L.S. de Saldarriaga, C. Saldarriaga, M.E. Davis, Investigations into the nature of a silicoaluminophosphate with the faujasite structure, J. Am. Chem. Soc. (1987) 2686–2691.
- [56] C.S. Blackwell, R.L. Patton, Solid-state NMR of silicoaluminophosphate molecular sieves and aluminophosphate materials, J. Phys. Chem. (1988) 3965–3970.
- [57] B. Zibrowius, E. Löffler, M. Hunger, Multinuclear MAS NMR and IR spectroscopic study of silicon incorporation into SAPO-5, SAPO-31, and SAPO-34 molecular sieves, Zeolites 12 (1992) 167–174.
- [58] R. Vomscheid, M. Briend, M.J. Peltre, P.P. Man, D. Barthomeuf, Small-pore molecular sieves SAPO-34 and SAPO-44 with chabazite structure: A study of silicon incorporation, J. Phys. Chem. 98 (1994) 4878–4883.
- [59] Z. Li, J. Martínez-Triguero, J. Yu, A. Corma, Conversion of methanol to olefins: Stabilization of nanosized SAPO-34 by hydrothermal treatment, J. Catal. 329 (2015) 379–388.
- [60] A. Ghorbanpour, A. Gumidyala, L.C. Grabow, S.P. Crossley, J.D. Rimer, Epitaxial growth of ZSM-5@Silicalite-1: A coreshell zeolite designed with passivated surface acidity, ACS Nano 9 (2015) 4006–4016.
- [61] L. Karwacki, M.H.F. Kox, D.A.M. de Winter, M.R. Drury, J.D. Meeldijk, E. Stavitski, W. Schmidt, M. Mertens, P. Cubillas, N. John, A. Chan, N. Kahn, S.R. Bare, M. Anderson, J. Kornatowski, B.M. Weckhuysen, Morphology-dependent zeolite intergrowth structures leading to distinct internal and outer-surface molecular diffusion barriers, Nat. Mater. 8 (2009) 959–965.
- [62] D. Chandler, Introduction to Modern Statistical Mechanics, Oxford University Press, 1987.

- [63] J. Crank, The Mathematics of Diffusion, 2nd ed., Oxford University Press, 1975.
- [64] D.M. Ruthven, Principles of Adsorption and Adsorption Processes, John Wiley & Sons, Inc., 1984.
- [65] R. Khare, D. Millar, A. Bhan, A mechanistic basis for the effects of crystallite size on light olefin selectivity in methanol-to-hydrocarbons conversion on MFI, J. Catal. 321 (2015) 23–31.
- [66] L.S. Darken, Diffusion, mobility and their interrelation through free energy in binary metallic systems, Trans. AIME 175 (1948) 184–201.
- [67] R.M. Barrer, D.W. Brook, Molecular diffusion in chabazite, mordenite, and levynite, Trans. Faraday Soc. (1953) 1049–1059.
- [68] R.M. Barrer, J.A. Davies, Sorption in decationated zeolites: II. Simple paraffins in H-forms of chabazite and zeolite L, Proc. Roy. Soc. Lond. A 322 (1971) 1–19.
- [69] D.H. Olson, M.A. Camblor, L.A. Villaescusa, G.H. Kuehl, Light hydrocarbon sorption properties of pure silica Si-CHA and ITQ-3 and high silica ZSM-58, Micropor. Mesopor. Mater. 67 (2004) 27–33.
- [70] D. Cai, Y. Cui, Z. Jia, Y. Wang, F. Wei, High-precision diffusion measurement of ethane and propane over SAPO-34 zeolites for methanol-to-olefin process, Front. Chem. Sci. Eng. 12 (2018) 77–82.
- [71] D. Chen, H.P. Rebo, K. Moljord, A. Holmen, Methanol conversion to light olefins over SAPO-34: Sorption, diffusion, and catalytic reactions, Ind. Eng. Chem. Res. 38 (1999) 4241–4249.
- [72] A. Hwang, D. Prieto-Centurion, A. Bhan, Isotopic tracer studies of methanol-toolefins conversion over HSAPO-34: The role of the olefins-based catalytic cycle. I. Catal. 337 (2016) 52–56.
- [73] A. Hwang, A. Bhan, Bifunctional strategy coupling Y₂O₃-catalyzed alkanal decomposition with methanol-to-olefins catalysis for enhanced lifetime, ACS Catal. 7 (2017) 4417–4422.
- [74] W.M. Deen, Analysis of Transport Phenomena, 2nd ed., Oxford University Press, 2011.
- [75] G.F. Froment, K.B. Bischoff, J.D. Wilde, Chemical Reactor Analysis and Design, 3rd ed., Wiley, 2010.
- [76] R. Aris, Elementary Chemical Reactor Analysis, Prentice Hall, 1969.
- [77] E. Iglesia, S. Soled, J.E. Baumgartner, S.C. Reyes, Synthesis and catalytic properties of eggshell cobalt catalysts for the Fischer-Tropsch synthesis, J. Catal. 153 (1995) 108–122.
- [78] M.L. Sarazen, E. Doskocil, E. Iglesia, Effects of void environment and acid strength on alkene oligomerization selectivity, ACS Catal. 6 (2016) 7059–7070.

- [79] W. Knaeble, E. Iglesia, Acid strength and metal-acid proximity effects on methylcyclohexane ring contraction turnover rates and selectivities, J. Catal. 344 (2016) 817–830.
- [80] G. Noh, Z. Shi, S.I. Zones, E. Iglesia, Isomerization and β-scission reactions of alkanes on bifunctional metal-acid catalysts: Consequences of confinement and diffusional constraints on reactivity and selectivity, J. Catal. https://doi. org/10.1016/j.jcat.2018.03.033. (in press).
- [81] R. Khare, Z. Liu, Y. Han, A. Bhan, A mechanistic basis for the effect of aluminum content on ethene selectivity in methanol-to-hydrocarbons conversion on HZSM-5, J. Catal. 348 (2017) 300–305.
- [82] K.B. Bischoff, Effectiveness factors for general reaction rate forms, AIChE J. 11 (1965) 351–355.
- [83] E.W. Thiele, Relation between catalytic activity and size of particle, Ind. Eng. Chem. 31 (1939) 916–920.
- [84] M. Boudart, Turnover rates in heterogeneous catalysis, Chem. Rev. 95 (1995) 661–666
- [85] Y.V. Joshi, A. Bhan, K.T. Thomson, DFT-based reaction pathway analysis of hexadiene cyclization via carbenium ion intermediates: Mechanistic study of light alkane aromatization catalysis, J. Phys. Chem. B 108 (2004) 971–980.
- [86] Y.V. Joshi, K.T. Thomson, Embedded cluster (QM/MM) investigation of C6 diene cyclization in HZSM-5, J. Catal. 230 (2005) 440–463.
- [87] Y.V. Joshi, K.T. Thomson, Brønsted acid catalyzed cyclization of C7 and C8 dienes in HZSM-5: A hybrid QM/MM study and comparison with C6 diene cyclization, J. Phys. Chem. C 112 (2008) 12825–12833.
- [88] H. Ma, Y. Chen, Z. Wei, S. Wang, Z. Qin, M. Dong, J. Li, J. Wang, W. Fan, Reaction mechanism for direct cyclization of linear C5, C6, and C7 alkenes over H-ITQ-13 zeolite investigated using density functional theory, ChemPhysChem 19 (2018) 496–503.
- [89] I.M. Dahl, S. Kolboe, On the reaction mechanism for propene formation in the MTO reaction over SAPO-34, Catal. Lett. 20 (1993) 329–336.
- [90] I.M. Dahl, S. Kolboe, On the reaction mechanism for hydrocarbon formation from methanol over SAPO-34. 1. Isotopic labeling studies of the co-reaction of ethene and methanol, J. Catal. 149 (1994) 458–464.
- [91] S. Ilias, R. Khare, A. Malek, A. Bhan, A descriptor for the relative propagation of the aromatic- and olefin-based cycles in methanol-to-hydrocarbons conversion on H-ZSM-5, J. Catal. 303 (2013) 135–140.